Statistical Analysis of the AIAA Drag Prediction Workshop CFD Solutions

Joseph H. Morrison and Michael J. Hemsch
NASA Langley Research Center
Hampton, Virginia, 23681 USA

joseph.h.morrison@nasa.gov

ABSTRACT

The first AIAA Drag Prediction Workshop, held in June 2001, evaluated the results from an extensive N-version test of a collection of Reynolds-Averaged Navier-Stokes CFD codes. The code-to-code scatter was more than an order of magnitude larger than desired for design and experimental validation of cruise conditions for a subsonic transport configuration. The second AIAA Drag Prediction Workshop, held in June 2003, emphasized the determination of installed pylon-nacelle drag increments and grid refinement studies. The code-to-code scatter was significantly reduced compared to the first DPW, but still larger than desired. However, grid refinement studies showed no significant improvement in code-to-code scatter with increasing grid refinement. The third AIAA Drag Prediction Workshop, held in June 2006, focused on the determination of installed side-of-body fairing drag increments and grid refinement studies for clean attached flow on wing alone configurations and for separated flow on the DLR-F6 subsonic transport model. This report compares the transonic cruise prediction results of the second and third workshops using statistical analysis.

1.0 INTRODUCTION

The AIAA Applied Aerodynamics Technical Committee (APATC) has sponsored a series of three Drag Prediction Workshops for transonic cruise drag prediction of subsonic transports. The first Drag Prediction Workshop (DPW-I) was held in June 2001 [1,2], the second Drag Prediction Workshop (DPW-II) was held in June 2003 [3,4], and the third Drag Prediction Workshop (DPW-III) was held in June 2006 [5-9]. The objectives for these three workshops were (1) to assess the state-of-the-art computational methods as practical aerodynamic tools for aircraft force and moment prediction of industry relevant geometries, (2) to provide an impartial forum for evaluating the effectiveness of existing computer codes and modeling techniques using Navier-Stokes solvers, and (3) to identify areas needing additional research and development.

DPW-I solicited CFD predictions of the lift, drag, and pitching moment for a subsonic transport wing-body configuration. The DLR-F4 wing-body configuration [10-12] was chosen due to public availability of the geometry and experimental data from three wind tunnels. The test cases consisted of a single point solution at a fixed value of C_L (C_L = 0.5±0.001), calculation of a drag polar, and an optional calculation of drag rise at a constant value of C_L. DPW-I did not require a grid convergence analysis. A total of 38 solutions were submitted for the workshop from 18 authors using 13 different CFD codes. A summary of the results of the workshop is given in Ref. 1 and a statistical analysis of the results is given in Ref. 2. The code-to-code statistical analysis of the results identified two major surprises [2]: (1) roughly 20% of the solutions were statistical outliers compared to the others and (2) the code-to-code scatter for drag was more than an order of

magnitude larger than the one drag count desired by airframe designers.

DPW-II focused on the prediction of installed pylon-nacelle drag increments and on grid refinement studies. The DLR-F6 [13] Wing-Body and Wing-Body-Nacelle-Pylon configurations were chosen for DPW-II since DLR and ONERA made data publicly available for this configuration. The test cases consisted of a single point solution at a fixed value of C_L (C_L = 0.5±0.001) for both the DLR-F6 Wing-Body and Wing-Body-Nacelle-Pylon configurations on coarse, medium, and fine grids, and a drag polar. Optional test cases included a comparison of tripped and fully turbulent solutions and calculation of drag rise at a fixed value of C_L. A total of 21 solutions were submitted for the workshop from 20 authors using 18 different CFD codes. There were 16 solutions that calculated all three grid levels for both the DLR-F6 Wing-Body and Wing-Body-Nacelle-Pylon from 15 authors using 15 different CFD codes. A summary of the results is given in Ref. 3 and a statistical analysis of the results is given in Ref. 4. The DLR-F6 configuration had substantial areas of separation at the wing-body juncture and at the wing-pylon juncture. Additionally, there was a region of separation at the trailing edge of the wing. The code-to-code scatter was significantly reduced from DPW-I although it was still an order of magnitude larger than desired by airframe designers. However, there was no significant change in code-to-code scatter with increasing grid density.

The discussion at DPW-II identified three suggestions for DPW-III: (1) test cases should be chosen with minimal separation since the large regions of separation were a likely culprit for the lack of grid convergence, (2) simpler cases were required to allow for better grid convergence studies and wider participation, and (3) blind studies were preferable where experimental data were not available *a priori*. It was generally agreed that continuing studies of the DLR-F6 case were warranted. Therefore, Vassberg *et al.* [14] designed a side-of-body fairing for the DLR-F6, designated the FX2B, to remove the wing-body juncture separation. Additionally, two wings, DPW-W1 and DPW-W2, were designed (see Ref. 5 for a description of this process) for a simple geometry with DPW-W2 a single point optimization of DPW-W1. A summary of the results from DPW-III is provided in Ref. 5. Detailed results from participants are provided in Refs. 6-9.

This paper is organized in the following manner. Section II provides a description of the statistical analysis. Section III outlines the test cases for the DPW-III workshop. Section IV provides the statistical results for the DPW-III test cases and statistical trends from all three workshops. Section V provides some summary comments.

2.0 STATISTICAL APPROACH

Hemsch [2] introduced the idea of treating different computations of a test case as a collective and using N-version testing in a statistical framework to investigate the submissions. No individual result is considered the "right" or "best" result. The dispersion of the results is treated as noise in the collective computational process.

A running record of individual outcomes is plotted for each of the measures of interest and derived quantities reported by participants. For DPW-I, DPW-II, and DPW-III Test Case 1, participants reported the angle of attack (α), total drag coefficient (C_D), pressure drag coefficient ($C_{D_{PR}}$), skin friction drag coefficient ($C_{D_{SF}}$), and moment coefficient (C_m). Since DPW-III Test Case 2 was a fixed angle-of-attack case, participants reported the lift coefficient (C_L), total drag coefficient, pressure drag coefficient, skin friction drag coefficient, and moment coefficient. The derived measures of interest were the lift-to-drag ratio (C_L/C_D) and idealized profile drag ($C_{DP} = C_D - C_L^2/\pi AR$), where AR is the wing aspect ratio. The value of the measure of

interest is plotted on the vertical axis and an integer index is used for each data submission on the horizontal index. The submissions are grouped according to grid type (multi-block structured, overset structured, unstructured).

An estimate of the population mean, $\hat{\mu}$, of the plotted data submissions is made and is shown on each graph as the centerline. Upper and lower scatter limits are then placed on the graphs as follows:

$$\text{Upper Limit} = \hat{\mu} + K\hat{\sigma} \qquad (1)$$

$$\text{Lower Limit} = \hat{\mu} - K\hat{\sigma} \qquad (2)$$

where $\hat{\sigma}$ is an estimate of the population standard deviation and K is an appropriate coverage factor. Significant results are outcomes that lie outside the process limits defined in Eqs. (1) and (2). These results, referred to as outliers, represent submissions that are different from the results that lie within the scatter limits. The outlier submissions should be investigated to understand the cause of the significant differences.

The population mean, $\hat{\mu}$, is estimated using the sample median, which is given (for sorted data) as:

$$\hat{\mu} = \tilde{x}$$

$$\tilde{x} \equiv x_{(n+1)/2} \qquad \text{(n odd)} \qquad (3)$$

$$\tilde{x} \equiv 0.5(x_{n/2} + x_{(n/2)+1}) \qquad \text{(n even)}$$

The sample median is robust to outliers, meaning that it is a representative mean of the population, not skewed or unduly influenced by the outliers. The sample standard deviation

$$\hat{\sigma} = SSD \equiv \sqrt{\frac{1}{n-1}\sum_{i=1}^{n}(x_i - \bar{x})^2} \qquad (4)$$

is used to estimate the population standard deviation. The coverage factor is estimated for a uniform distribution [15] as $K = \sqrt{3}$.

3.0 DPW-III TEST CASES

Participants for DPW-III were given the option of calculating Case 1, Case 2, or both. All simulations were specified to be in free air, i.e. no wind tunnel walls or model support systems were to be included. The boundary layer was to be modeled as fully turbulent. Grids were made available for the three types (multi-block structured, overset structured, unstructured) or participants could provide their own grids. A summary of the grids and results is provided in Ref. 5. Additional details of individual grid families and results from participants are available in Refs. 6-9.

3.1 Case 1: DLR-F6 Wing-Body with and without FX2B Fairing

DPW-III Test Case 1 focused on the DLR-F6 Wing-Body configuration that was the subject of DPW-II. DPW-II matched the experimental Reynolds number of 3 million. DPW-III increased the Reynolds number to

5 million to reduce the region of wing trailing edge separation while remaining within the load limitations of the model. The DLR-F6 Wing-Body had a large separation at the aft wing-body juncture. Vassberg *et al.* [14] designed a side-of-body fairing, designated FX2B, that CFD results showed eliminated this separation. Participants were required to calculate the total drag coefficient, pressure drag coefficient, skin friction drag coefficient, and pitching moment coefficient for the DLR-F6 Wing-Body with and without the FX2B fairing. Participants were also required to report the separation data and pressure profiles for both configurations and angle of attack for the fixed C_L condition. The Case 1 studies were:

Flow Conditions for Single Point Grid Convergence Study with Three Grid Levels:

- Mach = 0.75
- $C_L = 0.5 \pm 0.001$
- Re = 5 million

Flow Conditions for Drag Polar on Medium Grid:

- Mach = 0.75
- Re = 5 million
- α = {-3.0, -2.0, -1.0, -0.5, 0.0, 0.5, 1.0, 1.5} degrees

3.2 Case 2: DPW-W1 and DPW-W2 Wing Alone

DPW-III Test Case 2 focused on the wing alone configurations. DPW-W2 is a single point optimization of the DPW-W1 wing. Both wings are simple trapezoidal wings with modern supercritical airfoil shapes. Participants were required to calculate the lift coefficient, total drag coefficient, pressure drag coefficient, skin friction drag coefficient, and pitching moment coefficient for both wings. Participants were also required to report the separation data and pressure profiles for both wings. The Case 2 studies were:

Flow Conditions for Single Point Grid Convergence Study with Four Grid Levels

- Mach = 0.76
- α = 0.5 degrees
- Re = 5 million

Flow Conditions for Drag Polar on Medium Grid

- Mach = 0.76
- Re = 5 million
- α = {-1.0, 0.0, 0.5, 1.0, 1.5, 2.0, 2.5, 3.0} degrees

4.0 RESULTS

The statistical analysis of Section 2.0 was performed for the Single Point Grid Convergence Studies of DPW-III Test Case 1, DPW-III Test Case 2, and DPW-II Wing-Body Test Case. More complete results are available in Ref. 16.

4.1 DPW-III Case 1: DLR-F6 and FX2B Wing-Body Grid Convergence Study

Twenty-six solutions were submitted for DPW-III Test Case 1. Not all of these solutions included the coarse, medium, and fine grid levels for both the DLR-F6 and FX2B configurations. The 20 submissions that did include all three grid levels for both configurations are termed the fully nested solutions. The statistical analysis identifies outliers that are different from the other solutions. The core solutions are the solutions that are similar to each other, i.e. the core solutions are the nested solutions minus the outliers. Table 1 summarizes the data submissions for the DLR-F6 results from DPW-II and Case 1 results from DPW-III. The DPW-III results include more submissions than DPW-II, but have slightly fewer authors, organizations, and CFD codes. The nested solutions used 9 turbulence models or variants and the core solutions used 8 turbulence models or variants.

Table 1: Comparison of workshop statistics for grid convergence of DLR-F6 wing/body configuration in DPW-II and DPW-III.

	DPW-II			DPW-III		
	Submissions	Nested	Core	Submissions	Nested	Core
Solutions	21	16	13	26	20	16
Authors	20	15	12	15	12	9
Institutions	16	14	11	13	10	9
Codes	18	15	12	14	12	8

4.1.1 Individuals Charts for Case 1 Grid Convergence Study

Running records of individual outcomes were plotted for each of the measures of interest, for each grid level in the grid resolution study, and for each configuration for a total of 42 plots for DPW-III Case 1 (7 measures of interest, 3 grid levels, 2 configurations). Not all of these will be shown here. Figure 1 shows the total drag coefficient for the DLR-F6 and FX2B configurations for the coarse, medium, and fine grid levels. The median, Eq. (3), is shown as a solid black line; scatter limits, Eqs. (1) and (2), are shown as dashed black lines. In all of the following plots for DPW-III Case 1, the solution index on the abscissa refers to the same solution submission.

Solution 2 is outside the scatter limits for the total drag coefficient for all three grid levels and for both the DLR-F6 and FX2B configurations. Three other solutions (16, 18, and 19) are outside the scatter limits for one of the configurations on one or more grid levels. Also note that the scatter level decreases as the grid is refined.

Figure 2 shows the fine grid pressure and skin friction drag coefficients for the FX2B configuration. Solution 2 is within the limits for the pressure drag, but the skin friction drag is high and outside the limits for all three grid levels for both the DLR-F6 and FX2B configurations (not all charts shown). (Solution 18 included the total drag coefficient but did not provide the pressure drag coefficient, skin friction drag coefficient, or the

pitching moment coefficient. Solution 18 is not plotted and is omitted from the calculation of statistics for those quantities that were not reported.)

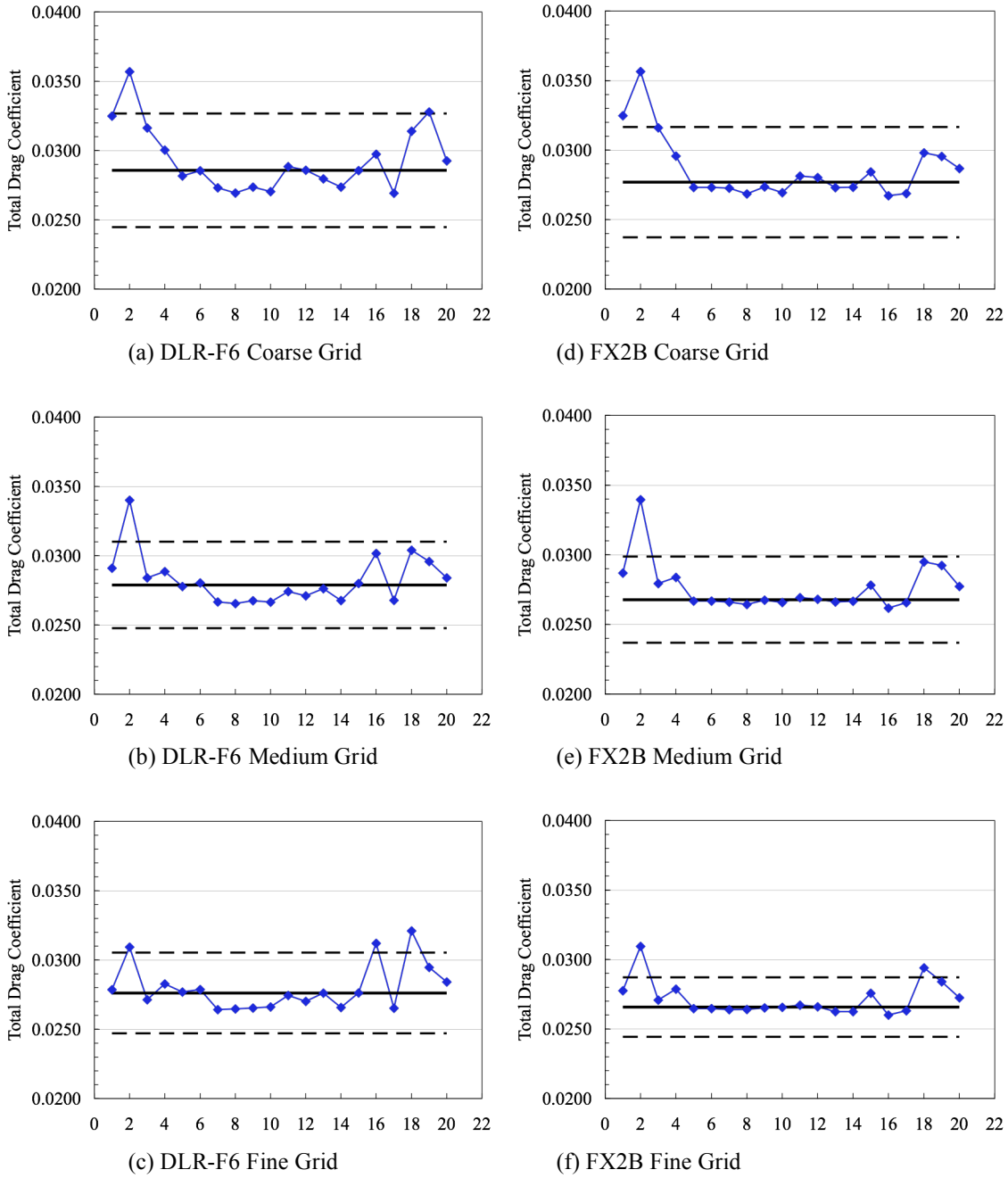

Figure 1: Comparison of individuals charts for the total drag coefficient for the DLR-F6 and the FX2B configurations for the cruise point grid convergence study.

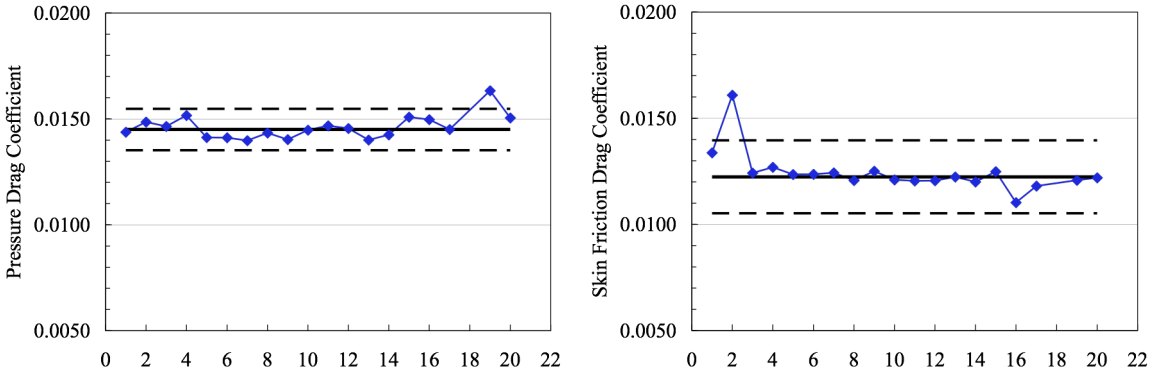

(a) Pressure drag coefficient (b) Skin friction coefficient

Figure 2: Comparison of individuals charts for the pressure drag coefficient and skin friction drag coefficient for the FX2B configuration fine grid.

Figure 3 shows the angle of attack and the pitching moment coefficient for the same fine grid solutions for the FX2B configuration. The angle of attack and moment coefficient for Solution 2 are very near the median. This is consistent with the pressure drag prediction. The difference in the total drag coefficient prediction of Solution 2 is clearly due to the skin friction.

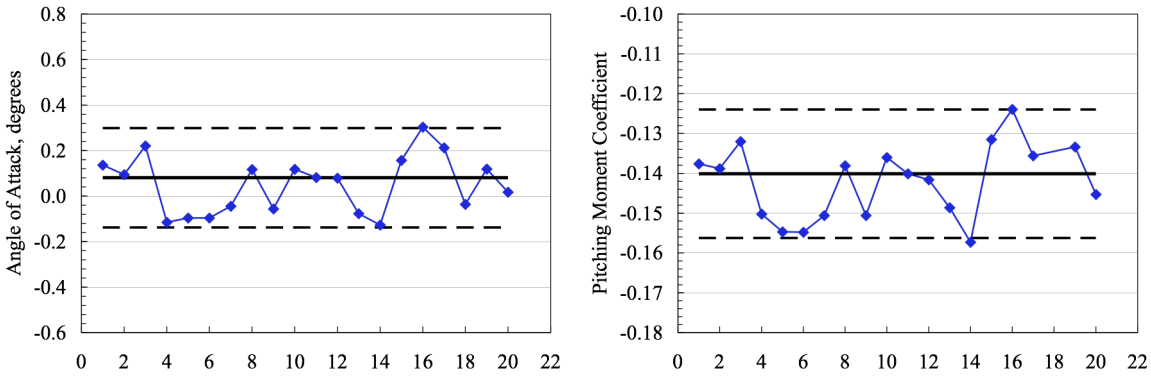

(a) Angle of attack (b) Pitching moment coefficient

Figure 3: Individuals charts for angle of attack and pitching moment coefficient for the FX2B configuration fine grid.

Solution 2 used the same grid, the same CFD code, and was provided by the same authors as Solutions 1 and 3. The difference between Solutions 1, 2, and 3 is solely the turbulence model. Solutions 1 and 3 used algebraic stress turbulence models; Solution 2 used a linear k-ε turbulence model. Clearly then, the k-ε turbulence model reported in Solution 2 predicts a different skin friction level than the other submissions.

4.1.2 Grid Convergence Results

It is difficult to see grid related trends in the data from the individuals charts. Therefore, all three grid levels were plotted together for each measure of interest for the DLR-F6 and FX2B configurations. The median and

scatter limits were included with the plots of variation. In order to compare results on unstructured meshes with results on multi-block structured meshes and overset structured meshes, it is convenient to use a one-dimensional estimate of the grid spacing

$$h = \frac{1}{\sqrt[3]{NPTS}}$$

where NPTS is the number of solution points (for either cell-centered or vertex based CFD codes) in the mesh. Coarse meshes show up on the right of the plot and finer grids approach the y-axis, which is the limit of infinite grid resolution, when plotted versus h^2 ($NPTS^{-2/3}$). It is often believed that second order accurate results will lie on a straight line when plotted versus $NPTS^{-2/3}$. Salas [17,18] has shown that the error is linear with h^p (where p is the order of accuracy of the scheme) only if the grid is refined uniformly in all coordinate directions, e.g. if the grid spacing is halved in the x coordinate, it must also be halved in the y and z coordinates. The gridding guidelines posted to guide development of grids for DPW-III (http://aaac.larc.nasa.gov/tsab/cfdlarc/aiaa-dpw/Workshop3/gridding_guidelines.html), included this as a requirement for structured grids for the DPW-III Case 2 Wing Alone grid convergence studies and as a recommendation for structured grids for DPW-III Case 1 DLR-F6 and FX2B due to the greater difficulty in generating these grids. The gridding guidelines required that the grid convergence cases maintain the same family of grids between grid levels. It was noted at the workshop that not all of the grids submitted for the workshop met these requirement. Therefore, plots for these grids will not necessarily achieve second order accuracy and will not show up as a straight line on these plots or even be monotonic.

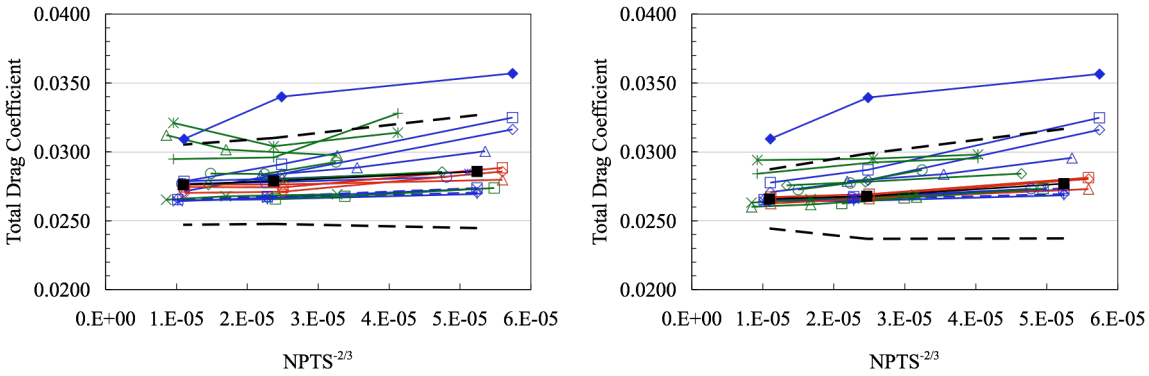

(a) DLR-F6 (b) FX2B

Figure 4: Grid convergence of total drag coefficient including mean and scatter limits.

In the following variation plots, the median is shown as solid black squares connected with a solid black line, the scatter limits are shown as dashed black lines, multi-block structured grids are plotted with blue symbols and lines, overset structured meshes are plotted with red symbols and lines, and unstructured meshes are plotted with green symbols and lines. Figure 4 shows the variation of the total drag coefficient for the nested solutions of both the DLR-F6 and FX2B configurations. Solution 2 (solid blue diamonds) is clearly outside the scatter limits confirming what was shown in Fig. 1. The reason for the difference in Solution 2 was determined in the previous section. The DLR-F6 total drag coefficient for Solutions 16 (green triangle) and 18 (green asterisk) increases as the grid is refined, falling outside the scatter limits for the finest grid, while the

other solutions decrease or remain constant.

Figure 5 shows the variation of the pressure drag coefficient for the DLR-F6 and FX2B configurations. Solution 16 is outside the scatter limits for the DLR-F6 and increases with mesh refinement. The pressure drag coefficient for Solution 16 is high but the skin friction drag is lower than the median resulting in the total drag coefficient falling within the scatter limits for all cases except the DLR-F6 fine grid. Solution 18, which showed a similar trend to Solution 16 for the total drag coefficient in Fig. 4, is not plotted as the drag component data were not provided. Solution 19 (green plus sign) distinctly falls outside the scatter limits for the pressure drag coefficient on the coarse mesh for DLR-F6 and all three mesh levels for FX2B. The scatter for the pressure drag coefficient decreases with grid refinement for the FX2B but not for the DLR-F6.

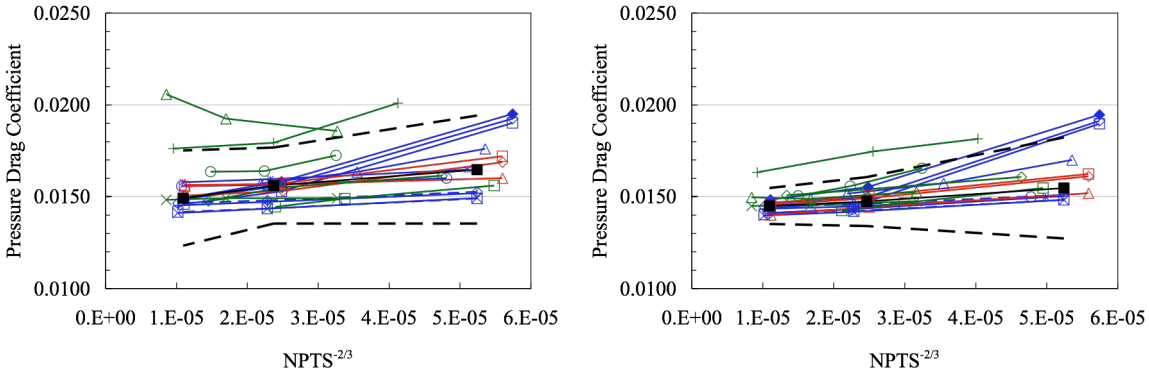

(a) DLR-F6 (b) FX2B

Figure 5: Grid convergence of pressure drag coefficient including mean and scatter limits.

Figure 6 shows the variation of the skin friction drag coefficient for all three grid levels of the DLR-F6 and FX2B. The skin friction drag coefficient for Solution 2 is high and well outside the scatter limits for all grid levels and both configurations. There is very little variation with grid level for most of the solutions for skin friction. The skin friction drag coefficient levels and grid variation are almost identical for each configuration.

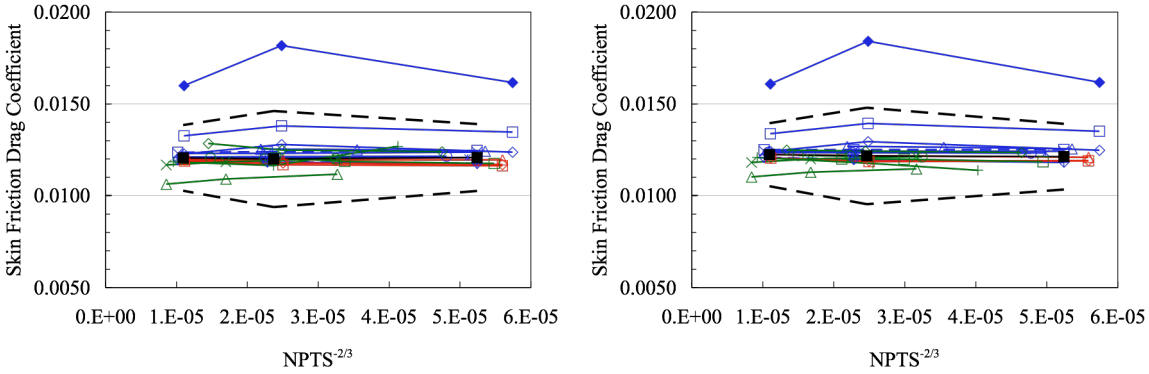

(a) DLR-F6 (b) FX2B

Figure 6: Grid convergence of skin friction drag coefficient including mean and scatter limits.

The variation of angle of attack for the DLR-F6, Fig. 7(a), is substantially larger than the variation for the FX2B, Fig. 7(b). The angle of attack for Solution 16 increases substantially with grid resolution for the DLR-F6. The angle of attack for Solution 18 decreases substantially for the finest grid on the DLR-F6.

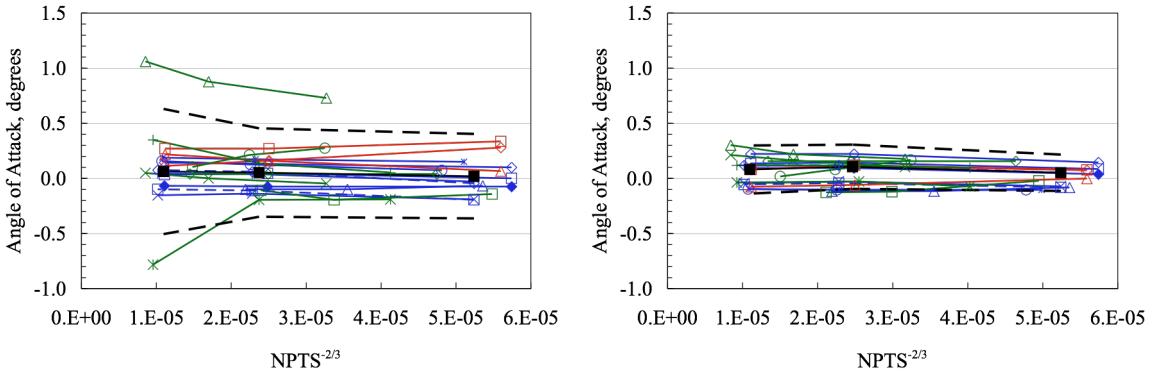

(a) DLR-F6 (b) FX2B

Figure 7: Grid convergence of angle of attack including mean and scatter limits.

The individuals charts in Fig. 1 and grid convergence charts in Figs. 4 and 6 show that the total drag coefficient and pressure drag coefficient for Solution 2 is consistently high and outside the scatter limits. Fig. 5(a) shows that the pressure drag coefficient for Solution 16 is high and outside the scatter limits and increases for the DLR-F6 configuration with increasing grid resolution. Fig. 5 shows that pressure drag coefficient is high for Solution 19 and outside the limits for the coarse grid on DLR-F6 and all grid levels for FX2B. Fig. 7 shows that Solutions 16 and 18 have different trends for angle of attack from the other solutions and are outside the scatter limits. Solution 18 showed a similar trend to Solution 16 for the total drag coefficient but drag components were not provided to see pressure and skin friction drag coefficients. The outliers were determined from this analysis to be these four solutions: 2, 16, 18, and 19.

It was previously shown that Solution 2 differs from the other solutions because of the turbulence model. It is not as clear why the unstructured Solutions 16, 18, and 19 differ from the core solutions. Solutions 16, 18, and 19 all used the Spalart-Allmaras (SA) turbulence model [18]; but so did Solutions 7, 9, 13, 14, 17, and 20 all of which are in the core. Solution 16 used the LaRC generated unstructured grid, but so did Solution 17 which is in the core. Solution 16 used an all tetrahedral mesh while Solution 17, which was in the core, used a hybrid mesh with the same grid points, but Solutions 18 and 19 used hybrid meshes and were outliers. Solutions 18 and 19 both used the same grids that were different from Solution 16 and Solution 18 had similar behavior for total drag coefficient as Solution 16. Solution 16 used full Navier-Stokes rather than the thin-layer assumption, but Solutions 9 and 10 also used full Navier-Stokes and were in the core. Furthermore, Solution 7 used the thin-layer assumption and Solution 9 used full Navier-Stokes with everything else the same and both were in the core. Solutions 8 and 10 also only differed in the thin-layer/full Navier-Stokes assumption and both were in the core. There does not appear to be a single main effect among the characteristics that were gathered that explain why these solutions differ from the other solutions. It is important to continue to investigate the cause of these differences in detail to identify improvements to CFD codes and solution processes.

4.1.3 Core Solutions

The core solutions are the 20 fully nested solutions minus the four outliers determined in the previous section (Solutions 2, 16, 18, and 19). The median values and standard deviations for the DPW-III Case 1 core solutions at all three grid levels are given in Ref. 16. The total drag variation of the core solutions is shown in Figure 8 including new estimates of the median and scatter limits for the core solutions. The variation of the core solutions is substantially reduced from the nested solutions. The variation of the core solutions for the total drag and pressure drag coefficients decreases with grid refinement and is more monotonic than the nested solutions.

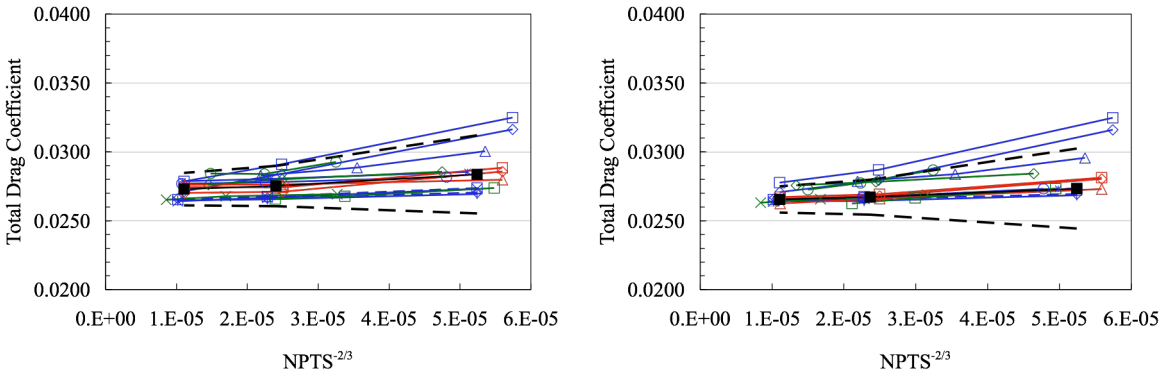

(a) DLR-F6 (b) FX2B

Figure 8: Comparison of total drag coefficient for core solutions including median and scatter limits.

4.2 DPW-III Case 2: DPW-W1 and DPW-W2 Wing Alone Grid Convergence Study

Twelve solutions were submitted for DPW-III Case 2. Ten of these solutions were nested, i.e. included all four grid levels for both the DPW-W1 and DPW-W2 wing configurations. Table 2 summarizes the data submissions for DPW-III Case 2. There were about half as many submissions for DPW-III Case 2 as there were for DPW-III Case 1. The nested solutions used 5 turbulence models or variants.

Running records of individual outcomes were plotted for each of the measures of interest, for each grid level in the grid resolution study, and for each configuration for a total of 56 plots for DPW-III Case 2 (7 measures of interest, 4 grid levels, 2 configurations). (Note that the index of solution is renumbered from DPW-III Case 1.) All of these individuals charts (not shown) were reviewed and no solutions were identified as clear outliers. Figure 9 and Figure 10 show the code-to-code scatter for the lift coefficient and the total drag coefficient. None of the solutions fall clearly outside of the scatter limits in a consistent pattern. Therefore, all of the nested solutions are determined to be in the core solutions. The scatter increases for all of these measures as the grid is refined. This is a surprising result since this is a simpler configuration than DPW-III Case 1. The scatter for DPW-III Case 1 decreased with increasing grid refinement.

Table 2: Comparison of workshop statistics for Case 2 wing alone grid configurations.

	DPW-W1 and DPW-W2 Wings	
	Submissions	Nested
Solutions	12	10
Authors	10	8
Institutions	8	7
Codes	8	7
Turbulence models and variants	6	5

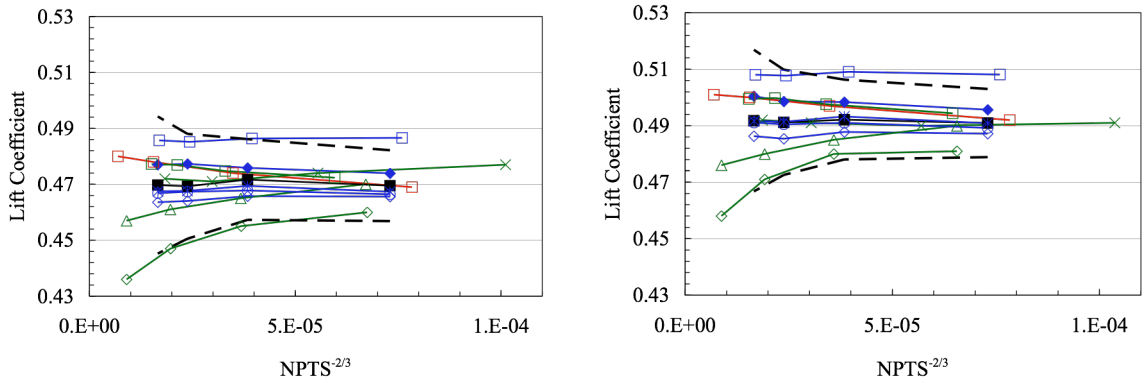

(a) DPW-W1 (b) DPW-W2

Figure 9: Comparison of lift coefficient for DPW-W1 and DPW-W2.

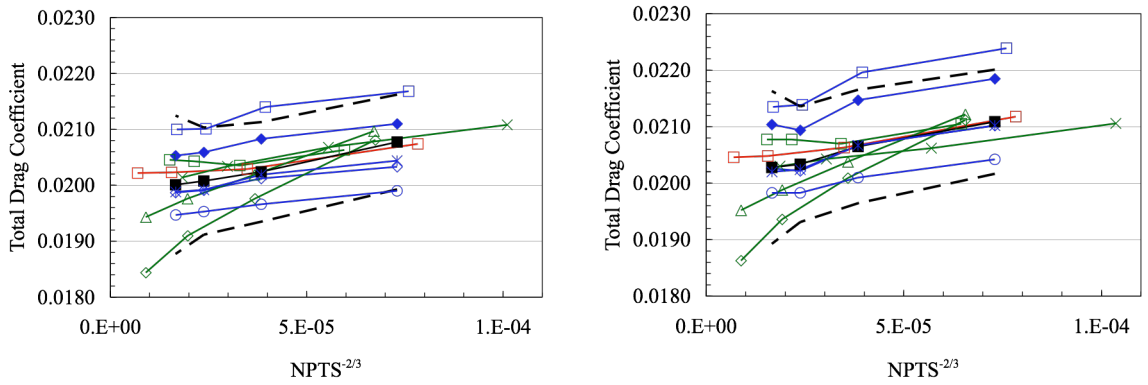

(a) DPW-W1 (b) DPW-W2

Figure 10: Comparison of total drag coefficient for DPW-W1 and DPW-W2.

DPW-III Case 2 was specified as a constant angle of attack case. The lift was a calculated value and varied as would be expected with solution and grid level. Fig. 9 shows the median and variation of the lift coefficient. The variation of the lift coefficient increases with increasing grid refinement. The drag has a component that is due to the lift. Therefore, a portion of the drag variation is due to the lift variation. Two derived quantities, the lift-to-drag ratio and the idealized profile drag coefficient, account in part for this variation of the lift in the drag. Figure 11 shows the variation in the lift-to-drag ratio for both the DPW-W1 and DPW-W2 wings. The median and scatter limits are also shown. The lift-to-drag ratio is higher for the DPW-W2 configuration, which was the one point optimization of DPW-W1. The variation is almost constant with grid refinement for both configurations, contrary to the increasing variation seen in the lift and total drag.

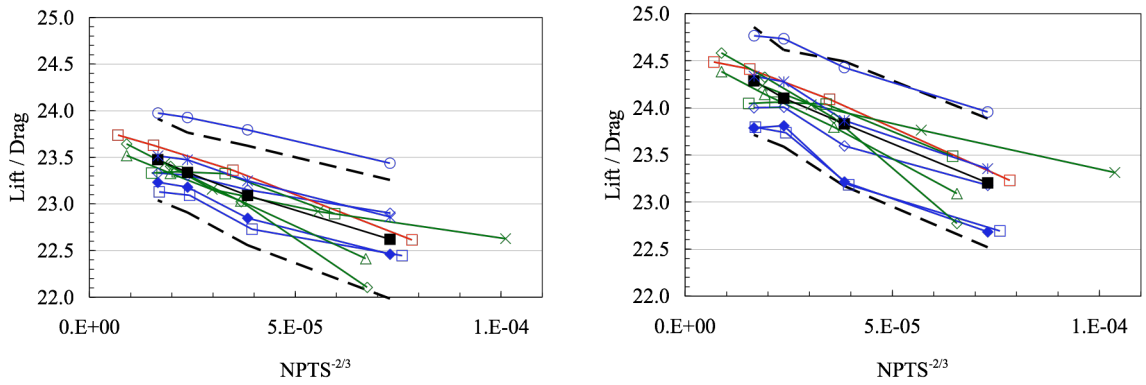

(a) DPW-W1 (b) DPW-W2

Figure 11: Comparison of lift-to-drag ratio for DPW-W1 and DPW-W2.

Figure 12 shows the variation in the idealized profile drag coefficient for both wing configurations. The idealized profile drag coefficient is lower for the optimized DPW-W2 configuration. The variation is again almost constant with grid refinement. Assessing the variation without accounting for the lift component of drag leads to a different result that the drag variation increases with grid refinement.

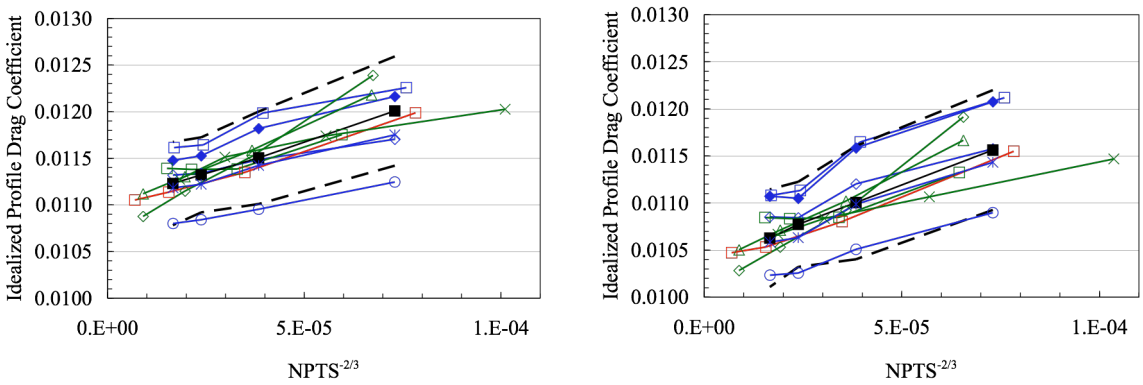

(a) DPW-W1 (b) DPW-W2

Figure 12: Comparison of idealized profile drag coefficient for DPW-W1 and DPW-W2.

The median values and standard deviations for the DPW-II Case 2 core solutions at all four grid levels are given in Ref. 16.

4.3 Comparison of DPW-II and DPW-III

The coefficient of variation [19], C_v (= σ/μ), provides a measure to compare the variation of populations with different means. Figure 13 compares the coefficient of variation of the total drag coefficient and the pitching moment coefficient for the five configurations considered, DPW-II DLR-F6 shown in green, DPW-III DLR-F6 shown as solid red lines and solid red symbols, DPW-III FX2B shown as dashed red lines and open red symbols, DPW-W1 shown as solid blue lines and solid blue symbols, and DPW-W2 shown as dashed blue lines and open blue symbols, across all grid levels (3 grid levels for DLR-F6 and FX2B; 4 grid levels for DPW-W1 and DPW-W2). The DPW-II DLR-F6 results are at Re = 3 million and the DPW-III DLR-F6 results are at Re = 5 million. The coefficient of variation for the total drag coefficient and pitching moment coefficient show similar trends:

- the variation for the DPW-III DLR-F6 and FX2B are very similar
- the variation of the DPW-W1 and the DPW-W2 are very similar
- the DPW-II DLR-F6 variation levels for total drag are lower than the DPW-III DLR-F6 and FX2B variation levels
- the DPW-II DLR-F6 variation levels are very near the levels of the DPW-W1 and DPW-W2
- the variation of the DPW-III DLR-F6 and FX2B is decreasing monotonically with increasing grid refinement
- the variation of the DPW-W1 and DPW-W2 wings is increasing with grid refinement
- the variation of DPW-II DLR-F6 is non-monotonic.

The standard deviation of total drag coefficient for the DPW-III DLR-F6 and FX2B configurations decreases from about 6% of the mean total drag coefficient on the coarse grid to about 2% on the fine grid. However, the standard deviation of the total drag coefficient for the DPW-W1 and DPW-W2 wing configurations increases from about 2% of the mean total drag coefficient on the coarse grid to about 4% of mean for the fine grid.

The standard deviation of the pitching moment coefficient for the DPW-III DLR-F6 and FX2B configurations decreases from about 9% of the mean pitching moment for the coarse grid to about 4.5-6% of the mean for the fine grid, with the DLR-F6 having the lower value of variation. The standard deviation for the pitching moment coefficient of the DPW-W1 and DPW-W2 wing configurations increases from about 3-3.5% of the mean pitching moment on the coarse grid to about 5.5% of the mean value on the fine grid.

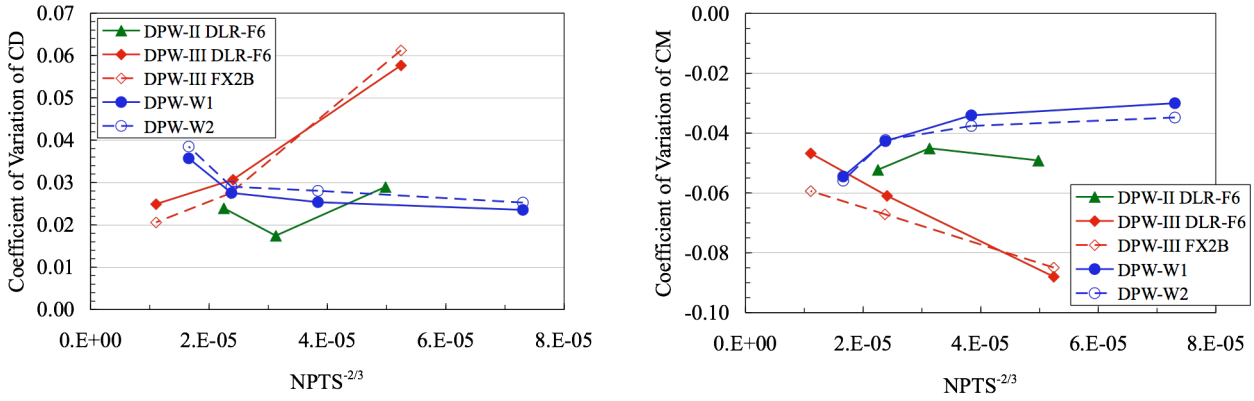

(a) Total Drag Coefficient

(b) Pitching Moment Coefficient

Figure 13: Comparison of coefficient of variation for total drag coefficient and pitching moment coefficient.

The coefficient of variation for the pressure and skin friction drag coefficients is shown in Figure 14. The trends for the pressure drag coefficient nearly mirror the total drag coefficient except (1) the variation of the pressure drag coefficient for the DPW-III DLR-F6 is noticeably larger than the FX2B for the fine grid (about 2.5% versus about 4.5% respectively) and (2) the variation of the pressure drag for the DPW-II DLR-F6 is closer to the variation for the DPW-III DLR-F6 than the total drag variation is. There is minimal variation in the skin friction drag for the DPW-W1 and DPW-W2 wing configurations except at the finest grid. The variation in the skin friction for the DPW-II DLR-F6, the DPW-III DLR-F6, and the FX2B configurations are almost indistinguishable and non-monotonic.

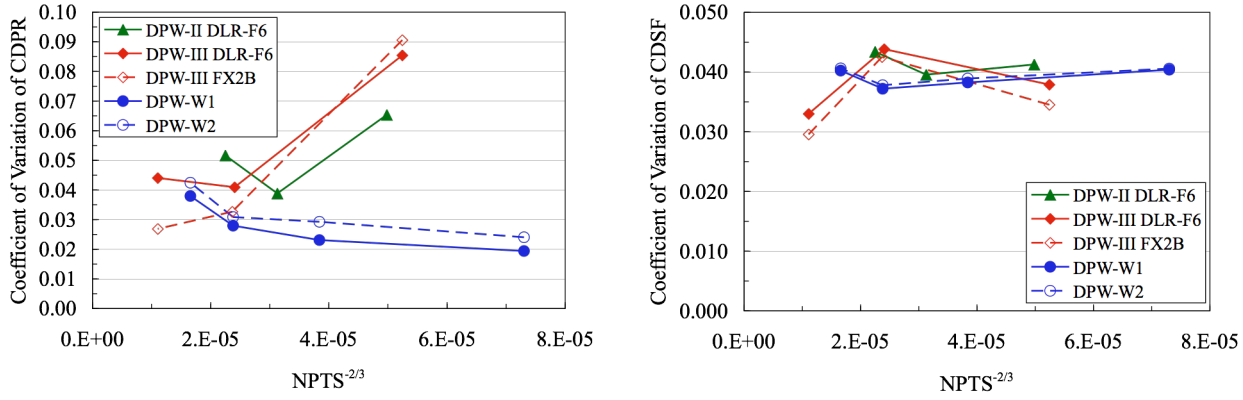

(a) Pressure Drag Coefficient

(b) Skin Friction Drag Coefficient

Figure 14: Comparison of coefficient of variation for pressure drag coefficient and skin friction drag coefficient.

DPW-III Case 1 was a constant lift case and DPW-III Case 2 was a constant angle of attack case. As discussed

earlier, the lift varied for DPW-III Case 2 and the drag has a component due to lift. Comparing the drag when the lift varies resulted in larger scatter for DPW-III Case 2 than was seen when the drag component due to lift was corrected. The two derived quantities, lift-to-drag ratio and idealized profile drag, give a better estimate of the variation at the same level of lift. Figure 15 shows the variation for the DPW-III DLR-F6, FX2B, DPW-W1, and DPW-W2 configurations. The variation for the DLR-F6 and FX2B look very similar to the total drag variation, but now the variation for the DPW-W1 and DPW-W2 is substantially smaller (approximately 1% of mean for lift-to-drag ratio and approximately 2-3% of mean for idealized profile drag) than the total drag coefficient. More interestingly, the variation for the DPW-W1 and DPW-W2 has very little change with grid refinement. The variation of DLR-F6 and FX2B still has a large decrease with increasing grid refinement.

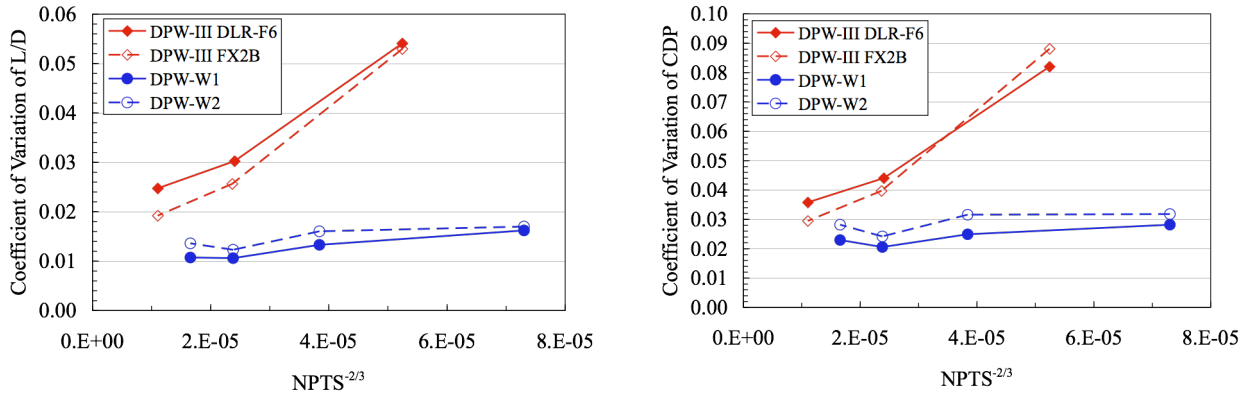

(a) Lift-to-Drag Ratio

(b) Idealized Profile Drag Coefficient

Figure 15: Comparison of coefficient of variation for lift-to-drag ratio and idealized profile drag.

The coefficient of variation for the lift-to-drag ratio and the idealized profile drag is substantially lower across all grid levels for the DPW-W1 and DPW-W2 wing configurations than the DLR-F6 and FX2B wing-body configurations. There is a minor reduction in variation for the FX2B configuration compared to the DLR-F6 which may not be statistically significant. The C_v plots for the pressure drag coefficient showed a similar decrease in variation for the FX2B from the DLR-F6 but the pitching moment coefficient showed a decrease in variation for the DLR-F6 compared to the FX2B.

Variation in the solutions is due to several factors including numerical error, differences in modeling (e.g. turbulence models), user effects (e.g. different levels of iterative convergence), and differences in CFD codes. Well constructed grid convergence studies provide a method to estimate the numerical error and to reduce the numerical error to any required level (limited only by resources and round-off error). DPW-III included grid convergence studies to address numerical errors. However, different models (8 different turbulence models were submitted for Case 1), user processes, and codes were represented. Unfortunately, not all possible combinations of these factors are included, limiting the ability to calculate main effects and higher-order interactions between effects. DPW-III Case 2 showed a nearly constant coefficient of variation independent of grid refinement. DPW-III Case 1 approached this value with grid refinement. Further studies would be required to determine if the level of variation achieved in DPW-III Case 2 and approached on the finest grid level in DPW-III Case 1 is the inherent variation due to these other factors when the numerical error is

negligible.

5.0 CONCLUDING REMARKS

The AIAA Drag Prediction Workshops have demonstrated the ability of state-of-the-art computational methods to predict transonic cruise drag of subsonic transports. The third Drag Prediction Workshop focused on blind tests of a wing-body configuration and a wing alone configuration to provide an impartial forum for evaluating Navier-Stokes solvers. There were no experimental data for any of the DPW-III cases that could be used to guide the solution process. The DLR-F6 and FX2B configurations for DPW-III Case 1 demonstrated a monotonic decrease in variation with increasing grid resolution; this is an improvement from DPW-II. However, the level of variation at the coarse and medium grid levels for DPW-II was lower for the total drag and pressure drag than the wing-body variation for DPW-III. The DPW-W1 and DPW-W2 demonstrated a nearly grid independent variation for total drag when the lift component was appropriately accounted for. The variation for the wing alone cases was significantly smaller for the coarser grids than the wing-body cases, but the variation for the wing-body cases approached the value of the variation for the wing alone cases at the highest grid resolution.

The variation for the core solutions of the DLR-F6 configuration, which included separation at the wing-body juncture, was approximately the same as the variation of the FX2B configuration, which had no separation at the wing-body juncture.

After three workshops, it is still clear that grids remain a first order effect and obtaining high quality grids is the first step to obtaining a high quality solution. Furthermore, obtaining a high quality family of grids for relatively simple wing-body configurations suitable for grid convergence studies remains a formidable challenge. Software tools to develop a family of grids rather than a single grid would provide an immense improvement in the CFD process.

The cause of the differences in the solutions was explored. The reason for one structured grid solution differing from the others was ascertained to be the use of a linear k-ε turbulence model. The cause of differences for three unstructured solutions is still unknown. It is imperative to investigate these outliers to identify why they are different in order to improve all CFD codes and processes.

[1] Levy, D. W., Zickuhr, T., Vassberg, J., Agrawal, S., Wahls, R. A., Pirzadeh, S., and Hemsch, M. J., "Data Summary from the First AIAA Computational Fluid Dynamics Drag Prediction Workshop," *Journal of Aircraft*, Vol. 40, No. 5, 2003, pp. 875- 882.

[2] Hemsch, M. J., "Statistical Analysis of Computational Fluid Dynamics Solutions from the Drag Prediction Workshop," *Journal of Aircraft*, Vol. 41, No. 1, 2004, pp. 95–103.

[3] Laflin, K. R., Klausmeyer, S. M., Zickuhr, T., Vassberg, J. C., Wahls, R. A., Morrison, J. H., Brodersen, O. P., Rakowitz, M. E., Tinoco, E. N., and Godard, J-L.,, "Data Summary from Second AIAA Computational Fluid Dynamics Drag Prediction Workshop," *Journal of Aircraft*, Vol. 42, No. 5, 2005, pp. 1165-1178.

[4] Hemsch, M. J., and Morrison, J. H., "Statistical Analysis of CFD Solutions from 2nd Drag Prediction Workshop," AIAA-2004-0556, January 2004.

[5] Vassberg, J. C., Tinoco, E. N., Mani, M., Brodersen, O. P., Eisfeld, B., Wahls, R. A., Morrison, J. H., Zickuhr, T., Laflin, K. R., and Mavriplis, D. J., "Summary of the Third AIAA CFD Drag Prediction Workshop," AIAA Paper 2007-0260, January 2007.

[6] Tinoco, E. N., Winkler, C., Mani, M., and Venkatakrishnan, V., "Structured and Unstructured Solvers for the 3rd CFD Drag Prediction Workshop," AIAA Paper 2007-0255, January 2007.

[7] Mavriplis, D. J., "Results from the 3rd Drag Prediction Workshop using the NSU3D Unstructured Mesh Solver," AIAA Paper 2007-0256, January 2007.

[8] Sclafani, A. J., Vassberg, J. C., Harrison, N. A., DeHaan, M. A., Rumsey, C. L., Rivers, S. M., and Morrison, J. H., "Drag Predictions for the DLR-F6 Wing/Body and DPW Wings Using CFL3D and OVERFLOW on an Overset Mesh," AIAA Paper 2007-0257, January 2007.

[9] Brodersen, O., Eisfled, B., Raddatz, J., and Frohnapfel, P., "DLR Results from the Third AIAA CFD Drag Prediction Workshop," AIAA Paper 2007-0259, January 2007.

[10] Redeker, G., "DLR-F4 Wing Body Configuration," in *A Selection of Experimental Test Cases for the Validation of CFD Codes*, AGARD-AR-303 Vol. II, August 1994, pp. B4.1-B4.21.

[11] Redeker, G., Muller, R., Ashill, P. R., Elsenaar, A., and Schmitt, V., "Experiments on the DLR-F4 Wing Body Configuration in Several European Wind Tunnels," in Chapter 2 of *Aerodynamic Data Accuracy and Quality: Requirements and Capabilities in Wind Tunnel Testing*, AGARD-CP-429, July 1988.

[12] Elsholz, E., "The DLR-F4 Wing/Body Configuration," in *ECARP - European Computational Aerodynamics Research Project: Validation of Turbulence Models*, *Notes on Numerical Fluid Mechanics*, Vol. 58, 1997, pp. 429-450.

[13] Brodersen, O., and Sturmer, A., "Drag Prediction of Engine-Airframe Interference Effects Using Unstructured Navier-Stokes Calculations," AIAA Paper 2001-2414, June 2001.

[14] Vassberg, J. C., Sclafani, A. J., and DeHaan, M. A., "A Wing-Body Fairing Design for the DLR-F6 Model: a DPW-III Case Study," AIAA Paper 2005-4730, June 2005.

[15] Anon., *U.S. Guide to the Expression of Uncertainty in Measurement*, ANSI/NCSL Z540.2-1997, October 1997, pp. 16-17.

[16] Morrison, J. H., and Hemsch, M. J., "Statistical Analysis of CFD Solutions from the Third AIAA Drag Prediction Workshop," AIAA Paper 2007-0254, January 2007.

[17] Salas, M. D., "Digital Flight: The Last CFD Aeronautical Grand Challenge," *Journal of Scientific Computing*, Vol. 28, Nos. 2/3, 2006, pp. 479-505.

[18] Salas, M. D., "Some Observations on Grid Convergence," *Computers & Fluids*, Vol. 35, No. 7, 2006, pp. 688-692.

[19] Spalart, P. R., and Allmaras, S. R., "A One-Equation Turbulence Model for Aerodynamic Flows," *La Recherche Aerospatiale*, No. 1, 1994, pp. 5-21.

[20] Wheeler, D. J., *Advanced Topics in Statistical Process Control*, SPC Press, Knoxville, TN, 1995.